Kinetic profiles and impurity transport response to 3D-field triggered ELMs in NSTX

F. Scotti[1], W. Guttenfelder[2], V.A. Soukhanovskii[1], R.E. Bell[2], G.P. Canal[4], J.M. Canik[3], A. Diallo[2], S.P. Gerhardt[2], S.M. Kaye[2], B.P. LeBlanc[2] and M. Podestà[2]

[1]Lawrence Livermore National Laboratory, Livermore CA 94550, USA
[2]Princeton Plasma Physics Laboratory, Princeton NJ 08543, USA
[3]Oak Ridge National Laboratory, Oak Ridge TN 37831, USA
[4]General Atomics, San Diego CA 92186-5608, USA

Corresponding Author: fscotti@pppl.gov

Abstract:
The response of kinetic plasma profiles to 3D-field triggered edge localized modes (ELMs) and the inter-ELM carbon impurity transport were analyzed in lithium-conditioned H-mode discharges in NSTX. Non-axisymmetric magnetic perturbations ($n = 3$) were applied in naturally ELM-free discharges to trigger ELMs (triggering frequency f_{ELM} = 10-60 Hz), and mitigate core impurity buildup maintaining the positive effects of lithium on energy confinement. Edge impurity flushing increased with f_{ELM}, with a progressive reduction in the carbon density n_C at the pedestal top. The changes in T_i profiles due to triggered ELMs led to changes in carbon neoclassical transport coefficients comparable and opposite to those observed in the transition from ELMy boronized discharges to ELM-free lithium-conditioned discharges. The agreement of inter-ELM carbon transport with neoclassical estimates improved with the increase in f_{ELM}. Quasi-linear fluxes from hybrid kinetic ballooning modes are shown to be of similar magnitude (but opposite direction) of the anomalous neoclassical fluxes in the ELM-free discharges.

1 Introduction

The ability to control the size and frequency (f_{ELM}) of edge localized modes (ELMs) will be critical in future fusion devices, in order to avoid impurity accumulation and damage to wall and divertor plasma facing components due to large ELMs. In the National Spherical Torus Experiment (NSTX), ELM-free lithium-conditioned H-mode discharges were characterized by core accumulation of impurities [1] as a result of near-neoclassical impurity transport, an edge inward impurity pinch and the absence of edge flushing mechanisms (e.g., ELMs, edge oscillations [2–5] and enhanced transport due to stochastic boundaries [6]). Accumulation of metal impurities led to core radiated power P_{rad} up to 50% of the injected power, while accumulation of carbon led to uncontrolled electron density n_e. The combined use of lithium coatings for deuterium control and ELM-triggering (via 3D-fields [7] or granule injection [8]) to flush core impurities is one of the candidate density control strategies for the NSTX-Upgrade (NSTX-U)[9] and therefore a better characterization of the operational regime and impurity transport is needed. Non-axisymmetric ($n = 3$) resonant magnetic perturbations (RMP) were applied in NSTX to trigger ELMs (f_{ELM} = 10-62.5 Hz), and mitigate core impurity buildup maintaining the positive effects of lithium on energy confinement. The triggering method and the effect on core plasma parameters has been extensively described in previous publications [7, 10–12]. This paper is dedicated to the analysis of the kinetic profiles evolution following triggered ELMs and to the characterization of impurity transport due to and following triggered ELMs.

2 Experimental setup and global parameters evolution

In NSTX, the triggering of ELMs via the application of 3D-field perturbations in naturally ELM-free discharges arrested the temporal evolution of global impurity parameters, such as impurity inventories and radiated power. In this paper, naturally ELM-free NSTX discharges with lithium conditioning (250 mg) are considered (see Ref. [11]). The discharges had plasma current I_p = 800 kA, neutral beam injected power P_{NBI}= 6 MW, strong shaping (triangularity δ = 0.8, elongation κ = 2.4) in a lower divertor biased double null configuration (δ_{r-sep} = -5-6 mm). Resonant magnetic perturbations ($n = 3$, 3 kA in coil current) were generated by the six ex-vessel midplane coils used for error field correction and applied for 4 ms starting at t = 0.4 s. Evolution of total core particle inventories (carbon and electrons) are shown in Figure 1 (a) and (b), respectively. ELM triggering and the increase in f_{ELM} led to a progressive reduction in electron and carbon total inventories until stationary values were achieved. MHD activity affected the discharge with the highest f_{ELM} starting from $t = 0.8$ s. Evolution of edge and core carbon inventories (outside and inside of $r/a = 0.5$, respectively, with r/a defined as the normalized half-width of the flux surface) are shown in Figure 1-(c-d) as a function of f_{ELM} at three different times: t = 0.35 s (before the start of ELM triggering), 0.65 s and 1.15 s. Separating the contribution to total particle inventories from core and edge plasma shows that the reduction in total inventories was due to a reduction in particle content in the plasma edge (by a factor of 2) while the core impurity content was unaffected, suggesting changes in impurity transport. The evolution of plasma kinetic profiles and core impurity transport is analyzed in detail in the following sections.

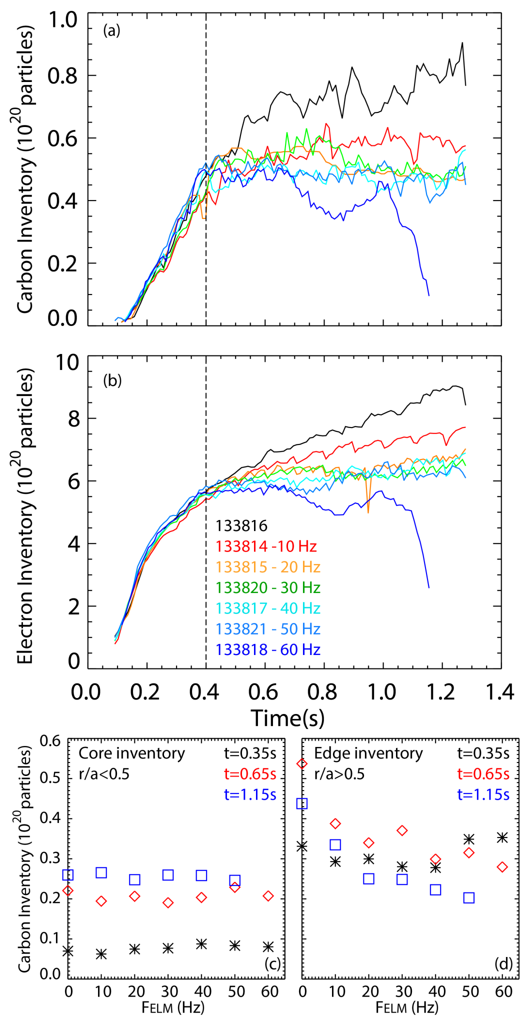

FIG. 1: Temporal evolution of carbon (a) and electron (b) particle inventories for increasing f_{ELM}. Core (c) and edge (d) carbon inventories as a function of f_{ELM} at t = 0.35 s (black), 0.65 s (red) and 1.15 s (blue).

3 Evolution of kinetic profiles due to RMP-triggered ELMs

Evolution of the pedestal electron and ion profiles was observed during the ELM cycle forced by the RMPs while the increase in f_{ELM} progressively affected the saturated plasma profiles (meaning, in this case, just before the next triggered ELM). Conditional averaging over the forced ELM cycles is employed to study the profile evolution recovering from the RMP ELM crash and to study profile changes as a function of triggered f_{ELM} for a given fraction of the forced ELM cycle. Modified hyperbolic tangent functions are used to fit the electron temperature T_e, density n_e, and pressure p_e profiles while spline fits are used for ion temperature T_i, toroidal velocity v_t and carbon density n_C [13].

For f_{ELM} = 10 Hz, the effect of the ELM crash was observed on all the kinetic profiles, with the largest drop on p_e, v_t and T_i (up to 40% at normalized poloidal flux $\psi_N = 0.7 - 0.8$). In Figure 2, n_e, T_e, p_e and T_i profiles are shown at different fractions of the ELM cycle. The changes in the profiles are to be attributed to the ELM crash as RMPs with amplitude below the ELM-triggering threshold had marginal effects on the plasma [12]. The profiles recovered to the before-ELM values only towards the end of the 100 ms cycle. A quick recovery of the steep gradient region in the electron profiles was observed, with a slower recovery of the pedestal top. The increase in f_{ELM} led to progressively smaller effects on the pedestal profiles, resulting in the reduced drop in stored energy associated with higher frequency triggered ELMs in Ref. [11]. The saturated profiles for the highest f_{ELM} cases asymptoted to the immediately post-ELM profiles observed at low triggering frequency.

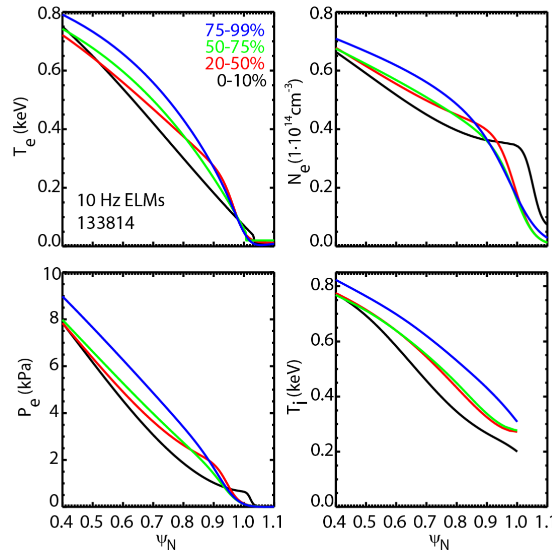

FIG. 2: Evolution of kinetic profiles following triggered ELMs with f_{ELM} = 10 Hz for different fractions of the paced ELM cycle.

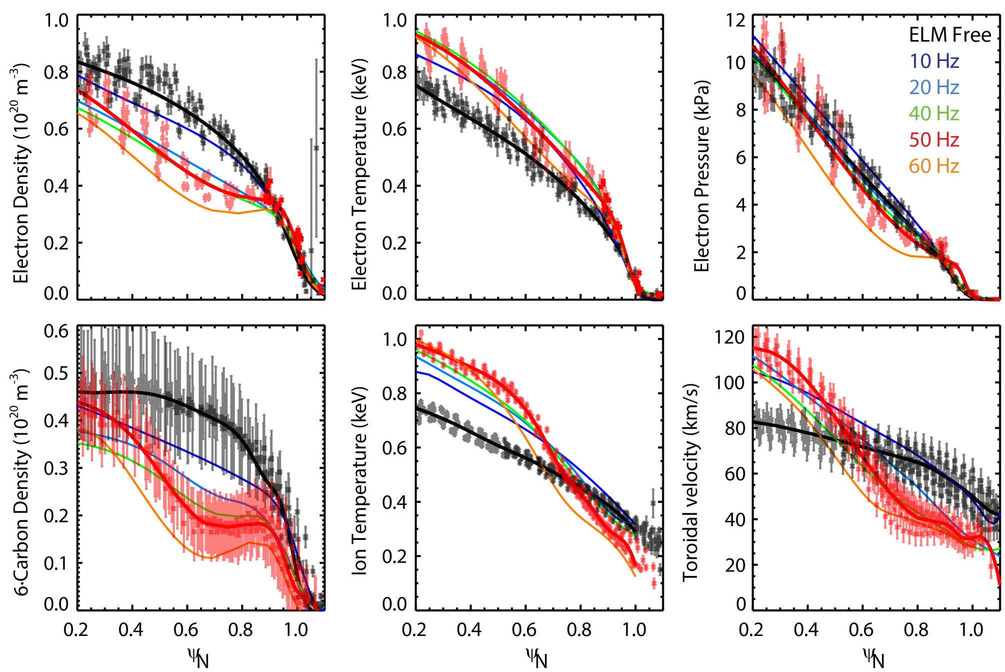

FIG. 3: Evolution of saturated kinetic profiles for increasing ELM triggering frequency.

The increase in f_{ELM} progressively affected inter-ELM kinetic profiles. Profiles for the 75%-99% of the paced ELM cycle are now considered for the different ELM triggering frequencies and shown in

Figure 3. While T_e profiles increased with higher f_{ELM}, n_e was reduced up to 40% at ψ_N = 0.6-0.7 with respect to the ELM-free case. In the last 25% of the ELM cycle, the steep gradient region for the electron profiles (0.9 $\leq \psi_N \leq$ 1.0) was unchanged in all the discharges in consideration (f_{ELM} = 0-60 Hz). A different behavior was observed for the evolution of v_t and T_i. For both quantities, higher core values and reduced edge values were observed, resulting in an increase in the temperature and velocity gradients in the region around ψ_N = 0.6-0.8 with normalized gradient scale length reduced by a factor 3-4. The changes in edge ion temperature and ion temperature gradient can have important consequences for edge ion collisionality and the neoclassical transport term commonly indicated as the "temperature screening" term [14].

Edge impurity flushing increased with f_{ELM}, with a progressive reduction in the carbon density n_C inside the pedestal top. For ELMs triggered at 10Hz, up to a 30% drop in n_C was observed for $\psi_N \geq 0.5$ following the ELM crash. Given the 100 Hz frame rate and the 7.4 ms integration time on the charge exchange recombination spectroscopy diagnostic used for the carbon density measurements, the steep gradient region in the n_C profiles already recovered in the first after-ELM frame. While n_C profiles recovered within the 100 ms ELM cycle, the increase in f_{ELM} led to a reduction in the overall core carbon inventory N_C progressively affecting n_C at inner radii. As discussed before, N_C decreased by up to a factor of two for $r/a \geq 0.5$ with the increase in f_{ELM} while no decrease was observed inside $r/a \sim 0.5$. These changes can be observed in Figure 4 where contour plots of carbon density versus time and radius are shown based on EFIT02 reconstructions for the ELM-free, 10 Hz and 50 Hz discharges. The observed changes in carbon density profile shape (in Figure 3 and 4) indicate a change in impurity transport for 0.4$\leq \psi_N \leq$0.8 induced by the ELM-triggering that goes beyond the simple periodic flushing and motivated the analysis presented in the next section.

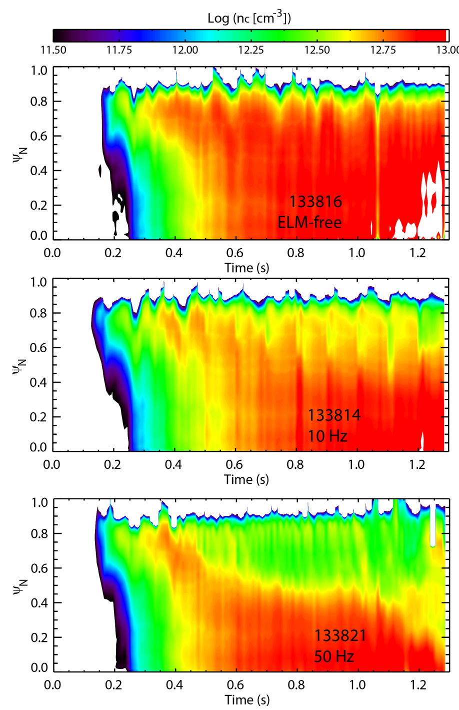

FIG. 4: Carbon density evolution as a function of radius and time for the ELM-free, 10 Hz and 50 Hz cases.

4 Impurity transport and consistency with neoclassical estimates

In NSTX, ion transport (both thermal and intrinsic impurities) was observed to be close to the neoclassical levels in H-mode discharges [1, 15, 16], with deviations observed at the plasma edge with lithium conditioning [1, 17]. In this work, neoclassical transport is evaluated with the drift-kinetic δf code NEO [18–20], which provides first principles numerical calculations of local neoclassical transport. NEO is run with experimental plasma profiles on equilibrium reconstructions from the kinetic EFITs. Input profiles are varied within the experimental error bars and the code is run 100 times on the spline-smoothed randomly-generated profiles to estimate uncertainty in the output neoclassical quantities. For each run a local scan in impurity gradient scale length is performed to infer transport coefficients from the radial fluxes calculated by NEO. Classical transport coefficients, not included in NEO but significant in NSTX, are estimated via the NCLASS module [21] in NEO and added to the neoclassical coefficients. In beam-heated NSTX plasmas, effects of toroidal rotation on impurity transport can be important. Finite rotation effects are included in the NEO simulations but are observed to be marginal in the discharges considered in this paper, where toroidal rotation was less than a factor of 1.5 higher than the thermal carbon velocity. Poloidal asymmetries are estimated to be up to 10-15% in the difference between inboard and outboard profiles and limited to the core of the plasma (r/a ≤ 0.4). Enhancement of transport coefficients due to centrifugal effects was typically observed for r/a ≤ 0.4, with an enhancement in radial carbon particle diffusivity of less than 30%. Modifications to the flux-surface averaged transport coefficients due to in-out asymmetries [22] (needed for interpretive runs with flux surface averaged codes like MIST [23]) were considered and found to be negligible.

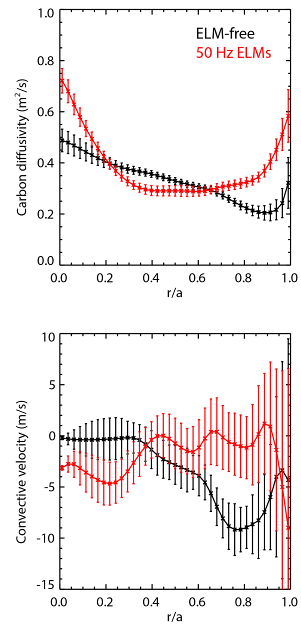

FIG. 5: Neoclassical carbon transport coefficients for ELM-free (black) and f_{ELM} = 50 Hz cases (red).

Changes in the carbon neoclassical transport coefficients (particle diffusivity D_C and convective velocity v_C) were observed with the increase in f_{ELM} and were opposite to those observed with the transition from naturally-ELMy discharges with boronized walls to lithium-conditioned ELM-free regimes [1]. In NSTX H-mode discharges, intrinsic carbon transport was consistent with neoclassical estimates in ELMy discharges with boronized PFCs. Changes in T_i, n_D profiles resulting from the application of lithium as wall conditioning led to changes in carbon neoclassical convection. However, a deviation of carbon transport from neoclassical estimates was evident at the top of the pedestal, where a predicted inward pinch was not observed experimentally. As discussed in the previous section, the application of 3D-field triggered ELMs to naturally ELM-free discharges led to changes in n_e, T_i, v_t. The changes in T_i and n_D profiles due to triggered ELMs led to changes in carbon neoclassical transport coefficients. In particular, the increased ion temperature gradient in the Pfirsch-Schlüter dominated edge region increased the outward convective component which compensated the deuterium density gradient driven pinch, resulting in a sign change in v_C at the top of the pedestal (from inward to outward convection). Changes in the diffusion coefficients and convective velocity are shown in Figure 5 for the ELM-free and the f_{ELM}= 50 Hz cases.

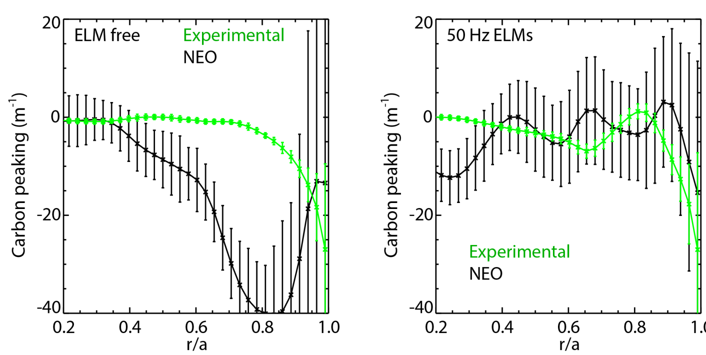

FIG. 6: Neoclassical (black) and experimental (green) carbon peaking factor for ELM-free (left) and f_{ELM} = 50 Hz cases (right).

The agreement of inter-ELM carbon transport with neoclassical estimates at the top of the pedestal improved with the increase in f_{ELM}, similarly to what observed in naturally ELMy discharges [1]. The ratio of neoclassical radial convective velocity to particle diffusivity is compared to the experimental carbon density peaking factor (inverse gradient scale length $L_{n_C}^{-1}$) to estimate the agreement of neoclassical transport with the experimental transport levels. In Figure 6, the experimental peaking factors, which in steady state in a source-free region are equal to the ratio of the effective convective and diffusive transport coefficients, are plotted together with the neoclassical estimates for v/D. The ELM-free discharge shows deviations between experimental transport and neoclassical estimates at the pedestal top with neoclassical transport predicting a strong conventionally-peaked carbon profile shape which is not observed experimentally. This anomaly is in line with what previously observed [1]. In the discharges with triggered ELMs a better agreement with neoclassical estimates is observed at the pedestal top with a hollow carbon density profile region due to the ion temperature driven component of the Pfirsch-Schlüter fluxes. In the steep gradient region both the ELM-free and ELMy cases are consistent with neoclassical estimates for the density peaking with the larger uncertainties associated to the flux component driven by the gradient of the deuterium density (not directly measured), resulting from the large carbon fraction in NSTX. These observations join lithium-conditioned discharges with triggered-ELMs and boronized naturally ELMy discharges with the comparable changes in the ion temperature profiles across both transitions. Possible reasons for the anomaly observed in the ELM-free discharges are further discussed in the next section. Also, it should be noted that the steady state analysis presented in this section (i.e., comparison of experimental and neoclassical peaking factors), only provides a necessary condition for consistency with neoclassical transport. The absolute values of the transport coefficients can only be inferred from time-dependent, perturbative studies. Initial attempts are presented in the last section.

5 Changes in ion scale turbulence

To assess possible anomalous contributions to the impurity particle flux, linear gyrokinetic analyses of the ELM-free and the f_{ELM} = 50 Hz discharges have been carried out. The linear GYRO [24] simulations utilize the numerical equilibria from the kinetic EFITs described above, and include kinetic deuterium, carbon and electron species as well as collisional and fully electromagnetic effects.

For the ELM-free discharge there is a broad spectrum of unstable microtearing modes at ion scale wavelengths ($k_\theta \rho_s < 1$) present in the region of r/a = 0.5-0.75 which is often found in NSTX H-modes [25]. These modes contribute only to electron heat flux and are not expected to influence the carbon density profile. Farther out (r/a = 0.8, 0.85) unstable ballooning modes exist that have the character of a hybrid kinetic ballooning mode reported in previous works [25–27]. These modes do contribute to heat, particle and momentum fluxes and can be considered as possible candidates that influence the carbon density profile. For the 50 Hz triggered-ELM case there is very little evidence for microtearing modes and instead there is a broad region of mixed ballooning mode activity, all of which can contribute to the carbon transport.

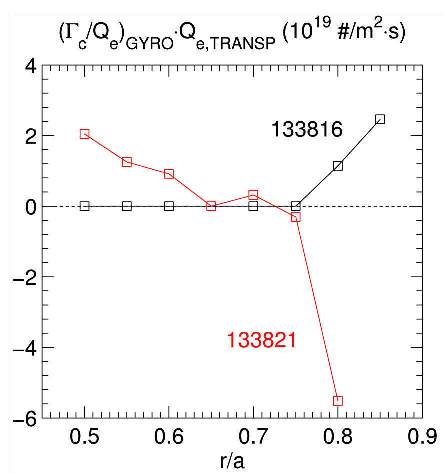

FIG. 7: Quasi-linear carbon fluxes, averaged over wavenumber $k_\theta \rho_s < 1$, and scaled by experimental TRANSP electron heat flux for the ELM-free discharge and 50 Hz ELM-paced discharge

While the linear simulations do not provide an absolute magnitude of transport, they do give the direction of particle flux (inward or outward) and the ratio of various fluxes, e.g., carbon particle flux to electron heat flux (Γ_c/Q_e). From the ratio of fluxes we can make an estimate of the magnitude of carbon fluxes that may be present due to the ballooning modes, which requires two key assumptions. First, we must assume the quasi-linear ratio of fluxes is similar to that predicted in the nonlinear turbulent state (often assumed in particle transport modeling, e.g. [22]). Second, we assume that the same instabilities are responsible for all of the electron heat flux, as determined from

TRANSP analysis ($Q_{e-GYRO} = Q_{e-TRANSP}$).

With these assumptions we can estimate the magnitude of carbon flux as $(\Gamma_c/Q_e)_{GYRO} \times Q_{e-TRANSP}$, which is shown in Fig. 7, averaged over unstable wavenumbers $k_\theta \rho_s < 1$. As expected, the microtearing modes produce negligible carbon flux in the ELM-free case over the region r/a = 0.5-0.75. However, the ballooning modes at 0.8-0.85 provide outward particle flux ($2-3 \times 10^{19}$ $m^{-2}s^{-1}$) that is similar in magnitude to the inward neoclassical pinch flux at the same location, which however extends between r/a = 0.65-0.9. In the triggered ELM case there is a similar outward transport of carbon further in (r/a = 0.5-0.65). However, the estimated flux is reduced to near zero around r/a = 0.75 and is inward directed at r/a = 0.8 suggesting that the anomalous contributions would lead to a carbon peaking at $r/a \sim$ 0.75, inconsistent with the neoclassical analysis above.

6 Time-dependent impurity transport studies

The time evolution of the n_C profiles following the 10 Hz triggered ELMs was used to try to estimate absolute values of experimental transport coefficients using the impurity transport code MIST [23]. Only a time-dependent analysis can be used to assess the consistency of absolute values of transport coefficients with the neoclassical estimates. Time-dependent MIST runs were used based on EFIT02 equilibria. Time dependent particle diffusivities were calculated using the NCLASS code and used as input to MIST. Convective velocities were adjusted to match the experimental carbon density profiles in the ELM-free reference discharge as done in Ref. [1]. The equilibrium v/D ratio was inferred from the steady state n_C profiles and the absolute convective velocity values were obtained assuming neoclassical diffusivity. Using neoclassical diffusivities and an anomalous convective velocity, MIST was able to reproduce the experimental carbon profile evolution, similarly to what was obtained in Ref. [1]. Transient perturbations to the steady state particle diffusivity D_C and convective velocity v_C were applied in MIST to simulate the response of the n_C profile to ELMs. Due to the charge exchange recombination spectroscopy system integration time, the first available profile is averaged over 10 ms after the ELM. At the first available charge exchange data point, the carbon density profile in the steep gradient region already recovered and the perturbation in transport coefficients in MIST was used effectively to create the starting point for the profile recovery study at inner radii. The experimentally observed increase in core n_C following the ELM was simulated with an inward convective perturbation for normalized volumetric radii R_{VOL} $\leq$0.6. An outward (diffusive/convective) perturbation for R_{VOL} $\geq$0.6 was used in the simulation to reproduce the edge ELM flushing. Experimental and MIST-simulated profiles before and after the ELM are shown in Figure 8-(top). After the ELM perturbation, carbon density profiles were allowed to recover using the steady state transport coefficients and the evolution of the MIST-simulated profiles was compared with the experimental one in Figure 8-(bottom). Experimental profiles are observed to recover on a timescale comparable but slower than the neoclassical timescale. The slower timescale would be consistent with transport coefficients smaller than the neoclassical values but can be interpreted as due to time varying transport

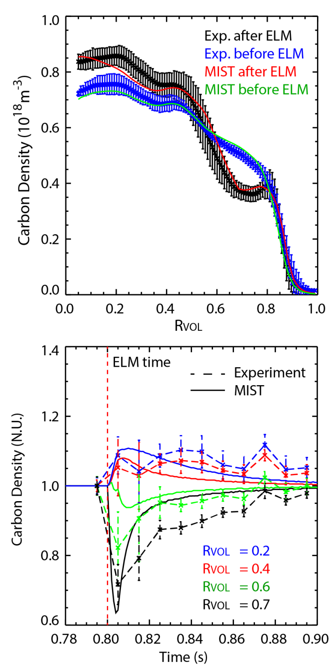

FIG. 8: Experimental and MIST-simulated carbon density profiles before and after a triggerd ELM (top); temporal evolution of normalized carbon density in experiment and MIST simulations (bottom).

coefficients, consistently with observations presented in Figure 2 where the recovery timescale of the profiles driving neoclassical transport was shown to be on the order of the ELM cycle itself.

7 Conclusions

The response of kinetic plasma profiles to RMP-triggered ELMs (f_{ELM}=10-60 Hz) and the inter-ELM carbon impurity transport were analyzed in naturally ELM-free lithium-conditioned H-mode discharges in NSTX. The triggering of ELMs arrested the temporal evolution of impurity inventories. The increase in f_{ELM} progressively affected inter-ELM kinetic profiles. n_e profiles for the 75%-99% of the paced ELM cycle were reduced up to 40% at ψ_N = 0.6-0.7 for f_{ELM} = 60 Hz, with respect to the ELM-free case. In the same region, a large increase in the ion temperature and toroidal velocity gradients was observed. Edge impurity flushing increased with f_{ELM}, with a progressive reduction in the carbon density n_C at the pedestal top. The changes in T_i profiles due to triggered ELMs led to changes in carbon neoclassical transport coefficients, with a sign change in the carbon convective velocity at the top of the pedestal (from inward to outward convection). The agreement of inter-ELM carbon transport with neoclassical estimates improved with the increase in f_{ELM}.

8 Acknowledgements

This work was supported by U.S. DOE Contracts: DE-AC02-09CH11466, DE-AC52-07NA27344, DE-AC05-00OR22725, DE-SC0012706.

References

[1] Scotti F, *et al.*, 2013 *Nucl. Fusion* **53** 083001
[2] Burrell K H, *et al.*, 2002 *Plasma Physics and Controlled Fusion* **44** A253
[3] Greenwald M, *et al.*, 2000 *Plasma Physics and Controlled Fusion* **42** A263
[4] Hu J S, *et al.*, 2015 *Phys. Rev. Lett.* **114**(5) 055001
[5] Osborne T, *et al.*, 2015 *Nuclear Fusion* **55** 063018
[6] Evans T E, *et al.*, 2004 *Phys. Rev. Lett.* **92**(23) 235003
[7] Canik J, *et al.*, 2010 *Phys. Rev. Lett.* **104** 045001
[8] Mansfield D, *et al.*, 2013 *Nuclear Fusion* **53** 113023
[9] Menard J, *et al.*, 2012 *Nuclear Fusion* **52** 083015
[10] Canik J, *et al.*, 2010 *Nuclear Fusion* **50** 034012
[11] Canik J, *et al.*, 2010 *Nuclear Fusion* **50** 064016
[12] Lore J, *et al.*, 2013 *Journal of Nuclear Materials* **438** S388 -S392
[13] Diallo A, *et al.*, 2011 *Nuclear Fusion* **51** 103031
[14] Hirshman S and Sigmar D, 1981 *Nucl. Fusion* **21 (9)** 1079
[15] Kaye S, *et al.*, 2007 *Nucl. Fusion* **47** 499–509
[16] Kaye S, *et al.*, 2009 *Nucl. Fusion* **49** 045010
[17] Kaye S, *et al.*, 2013 *Nucl. Fusion* **53** 063005
[18] Belli E and Candy J, 2008 *Plasma Phys. Control. Fusion* **50** 095010
[19] Belli E and Candy J, 2009 *Plasma Phys. Control. Fusion* **51** 075018
[20] Belli E and Candy J, 2012 *Plasma Phys. Control. Fusion* **54** 015015
[21] Houlberg W, *et al.*, 1997 *Phys. Plasmas* **4 (9)** 3230
[22] Angioni C, *et al.*, 2014 *Nuclear Fusion* **54** 083028
[23] Hulse R, 1983 *Nucl. Tech. Fusion* **3** 259
[24] Candy J, 2003 *J. Comput. Phys.* **186** 545
[25] Guttenfelder W, 2013 *Nucl. Fusion* **53** 093022
[26] Belli E, 2010 *Nucl. Fusion* **17** 112314
[27] Canik J, 2013 *Nucl. Fusion* **53** 113016